Optics Letters

Light and corona: guided-wave readout for coronavirus spike protein–host-receptor binding

Ilya V. Fedotov,[1,2,3,4] Zhenhuan Yi,[1] Aleksandr A. Voronin,[2,3,4] Anatoly A. Svidzinsky,[1] Kyle Sower,[1] Xinghua Liu,[1] Ekaterina Vlasova,[3] Tao Peng,[1] Xiangpei Liu,[1,5] Sergey A. Moiseev,[4] Vsevolod V. Belousov,[6,7] Alexei V. Sokolov,[1,8] Marlan O. Scully,[1,8,9] and Aleksei M. Zheltikov[1,2,3,4,*]

[1] *Institute for Quantum Science and Engineering, Department of Physics and Astronomy, Texas A&M University, College Station, Texas 77843, USA*
[2] *International Laser Center, Physics Department, M.V. Lomonosov Moscow State University, Moscow 119992, Russia*
[3] *Russian Quantum Center, Skolkovo, Moscow Region 143025, Russia*
[4] *Kazan Quantum Center, A.N. Tupolev Kazan National Research Technical University, Kazan 420126, Russia*
[5] *University of Science and Technology of China, Hefei 230026, China*
[6] *M. M. Shemyakin and Yu. A. Ovchinnikov Institute of Bioorganic Chemistry, Russian Academy of Sciences, Moscow 117997, Russia*
[7] *Federal Center of Brain Research and Neurotechnologies, Federal Medical Biological Agency, Moscow 117997, Russia*
[8] *Baylor University, Waco, Texas 76798, USA*
[9] *Princeton University, Princeton, New Jersey 08544, USA*
Corresponding author: zheltikov@physics.msu.ru

We show that waveguide sensors can enable a quantitative characterization of coronavirus spike glycoprotein–host-receptor binding—the process whereby coronaviruses enter human cells, causing disease. We demonstrate that such sensors can help quantify and eventually understand kinetic and thermodynamic properties of viruses that control their affinity to targeted cells, which is known to significantly vary in the course of virus evolution, e.g., from SARS-CoV to SARS-CoV-2, making the development of virus-specific drugs and vaccine difficult. With the binding rate constants and thermodynamic parameters as suggested by the latest SARS-CoV-2 research, optical sensors of SARS-CoV-2 spike protein–receptor binding may be within sight. © 2020 Optical Society of America

https://doi.org/10.1364/OL.402897

Advanced methods of guided-wave photonics and fiber optics offer unprecedented control over the spatial, temporal, spectral, and polarization structure of optical fields [1,2], providing unique resources for rapidly progressing optical technologies. Within the past two decades, these new concepts and approaches have been pushing the frontiers of ultrafast photonics and nonlinear optics, enabling multioctave supercontinuum generation [3], frequency-comb metrology [4]; subcycle lightwave electronics [5]; and quantum entanglement engineering [6]. The new reality of COVID-19, however, dictates its own priorities, promising no speedy return to the prepandemic normal. The focus of optical research is shifting toward responding to the urgent call for methods and concepts that would help

detect SARS-CoV-2 and contain the pandemic. Optical waveguide sensors have long been identified as powerful tools for virus detection [7–9]. Promising approaches to virus sensing include integrated waveguide Young interferometry [7], light scattering in nanofluidic optical fibers [8], and whispering gallery-mode microcavities [9].

Yet, truly connected to research performed directly on SARS-CoV-2 or SARS-CoV-2 pseudo-type viruses [10] are only, as of the time of this writing, optical methods based on surface plasmon resonance (SPR), optical density measurements in enzyme-linked immunosorbent assay (ELISA), and biolayer interferometry (BI). Here, we explore the ways to turn the tide for waveguide methods of biosensing.

As a central episode of coronavirus entry into a human cell [10], the spike (S) glycoprotein of the virus recognizes angiotensin-converting enzyme 2 (ACE2) in a targeted cell as its receptor and binds to ACE2, driving virus–membrane fusion. Even though, overall, SARS-CoV-2 shares this mechanism of viral entry with its earlier version, SARS-CoV, its receptor-binding domain (RBD) has been shown [10] to possess new structural and conformational features not observed in SARS-CoV, which provide additional binding sites, increasing the binding affinity of SARS-CoV-2 S protein to human ACE2 (hACE2). Understanding these new properties of SARS-CoV-2, including its higher receptor-binding affinity, is thus central for the development of effective, COVID-19-specific antibody drugs and a prophylactic vaccine.

Concentration $N_c(t)$ of the protein receptor complex that builds up on the surface as a result of this binding reaction is described by the rate equation $dN_c(t)/dt = k_1 N_s N_r - k_2 N_c$, where N_s and N_r are the protein and receptor concentrations, k_1
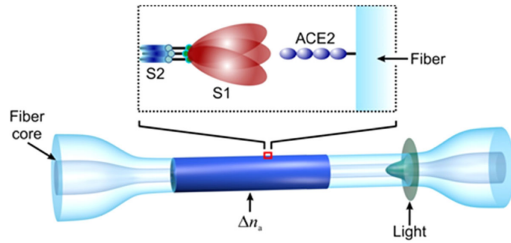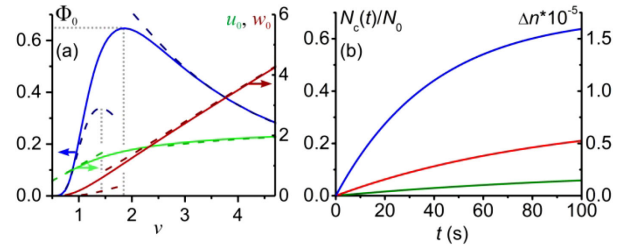
Fig. 1. Fiber taper with an index change Δn_a induced by protein receptor binding within a thin layer on the fiber-taper surface. Shown in the inset is SARS-CoV S protein–ACE2 receptor binding, giving rise to a protein–protein monolayer on the surface of the fiber taper.


Fig. 2. (a) Parameters u_0 and w_0 and the $\Phi_0(v)$ factor as functions of v found by solving the dispersion equation for the fundamental mode of a circular fiber (solid lines) and calculated as low and high v approximations, as defined in the text (dashed lines). The peaks of $\Phi_0(v)$ and $\Phi_c(v)$ at v_m and v_c are shown by the dotted lines. (b) Time dependences of N_c/N_0 (left axis) and Δn (right axis) for $N_s = 5$ nM (green curve), 20 nM (red curve), and 100 nM (blue curve) for surface-confined SARS-CoV-2-RBD–ACE2 protein receptor binding, with rate constants $k_1 \approx 1.75 \cdot 10^5$ M^{-1}s^{-1} and $k_2 \approx 7.75 \cdot 10^{-3}$ s^{-1}.

is the association rate for protein–receptor binding, and k_2 is the dissociation rate of the protein receptor complex. The buildup of $N_c(t)$ induces a change in the refractive index, Δn_a, within a thin layer near the receptor immobilization surface.

We now assume that this protein–receptor binding dynamic unfolds on the surface of an optical waveguide (Fig. 1). With no protein receptor complex layer on its surface, this waveguide confines light by a transverse refractive index profile $n(\mathbf{r})$, with $\mathbf{r} = (x, y)$. The eigenfunctions $\psi_j(\mathbf{r})$ and eigenvalues β_j of the modes guided by such an index profile are defined by the wave equation [11] $[\Delta_\perp + k^2 n^2(\mathbf{r}) - \beta_j^2]\psi_j(\mathbf{r}) = 0$, where $k = \omega/c = 2\pi c/\lambda$, ω is the frequency, λ is the wavelength, and c is the speed of light in vacuum.

To understand the effect of a protein receptor complex layer on the surface of such a waveguide, we consider a waveguide whose index profile is $\tilde{n}(\mathbf{r})$ and whose modal eigenfunctions $\tilde{\psi}_j(\mathbf{r})$ and eigenvalues $\tilde{\beta}_j$ are found from $[\Delta_\perp + k^2 \tilde{n}^2(\mathbf{r}) - \tilde{\beta}_j^2]\tilde{\psi}_j(\mathbf{r}) = 0$. The reciprocity relation [12] then dictates $\tilde{\beta}_j^2 - \beta_j^2 = k^2 [\int \psi_j(\mathbf{r}) \tilde{\psi}_j(\mathbf{r}) d\mathbf{r}]^{-1} \int [n^2(\mathbf{r}) - \tilde{n}^2(\mathbf{r})] \psi_j(\mathbf{r}) \tilde{\psi}_j(\mathbf{r}) d\mathbf{r}$, where the integration is over the entire xy-plane. For a weakly guiding structure, this integral equation can be solved for $\delta\beta_j = \tilde{\beta}_j - \beta_j$, leading to $\delta\beta_j \approx k\Omega_j$, where $\Omega_j = [\int \psi_j^2 d\mathbf{r}]^{-1} \int \Delta n \, \psi_j^2 d\mathbf{r}$ is the space overlap of the fiber mode and the refractive index change $\Delta n(\mathbf{r}) = \tilde{n}(\mathbf{r}) - n(\mathbf{r})$. This solution applies to a waveguide with any index profile $\tilde{n}(\mathbf{r})$, revealing a universal relation between the mode of eigenvalue shifts $\delta\beta_j$ and the overlap Ω_j.

We now focus on a fiber-optic setting (Fig. 1), taking $n(r) = n_1$ if $r = (x^2 + y^2)^{1/2} \le a$ and $n(r) = n_2$ if $r > a$ for a fiber with propagation constants β_j and eigenfunctions $\psi_j(\mathbf{r})$ and $\tilde{n}(r) = n_1$ if $r \le a$, $\tilde{n}(r) = n_2 + \Delta n_a$ if $a < r \le a + s$, and $\tilde{n}(r) = n_2$ if $r > a + s$ for a fiber with modal eigenfunctions $\tilde{\psi}_j(\mathbf{r})$ and eigenvalues $\tilde{\beta}_j$. With an index step defined now as $\Delta n(r) = \Delta n_a$ if $a \le r \le a + s$ and $\Delta n(r) = 0$ otherwise, space integration in the equation for Ω_j is within an $a \le r \le a + s$ ring, leading [11] to $\Omega_j = \Delta n_a(s/a)[\psi_j(r = a)]^2[\int \psi_j^2 r dr]^{-1}$. Aiming to isolate the effects of $|\Delta n|$ and s from the waveguiding factors, we represent the solution for $\delta\beta_j$ as $\delta\beta_j \approx k\Delta n_a(s/a)\Phi_j(v)$, with $\Phi_j = a\Omega_j/(s\Delta n_a)$ defined as the overlap Ω_j per unit Δn per unit s/a. For the index profile $n(r)$, as specified above, $\Phi_j(v) = 2(u_j/v)^2 K_l^2(w_j)[K_{l-1}(w_j)K_{l+1}(w_j)]^{-1}$, where $K_l(\xi)$ are the modified Bessel functions of the second kind, $v = ka(n_1^2 - n_2^2)^{1/2}$ is the waveguide parameter, l is the orbital mode index, $u_j = a(k^2 n_1^2 - \beta_j^2)^{1/2}$, and $w_j = a(\beta_j^2 - k^2 n_2^2)^{1/2}$.

For the fundamental mode, $j = 0$, the solution for $\delta\beta_j$ reduces to $\delta\beta_0 = 2 k(s/a)\Delta n_a(u_j/v)^2 K_0^2(w_j)[K_1(w_j)]^{-2}$. At high v, $u_0 \approx u_{01}\exp(-1/v)$ [green dashed line in Fig. 2(a)], with $u_{01} \approx 2.405$ defined as the first root of the zeroth-order Bessel function, $J_0(\xi) = 0$. In this regime, $\Phi_0(v) \approx 2(u_0/v)^2[w_0/(w_0 + 1)] \approx 2u_0^2[v(v + 1)]^{-1}$ [blue dashed line in Fig. 2(a)], leading to $\delta\beta_0 \approx 2 k\Delta n_a(s/a)u_0^2[v(v + 1)]^{-1}$, rapidly decreasing with v. The respective mode index change is $\delta n_0 = \delta\beta_0/k \ll (s/a)\Delta n_a \ll 1$. Since the field is tightly localized within the fiber core for high v, a small $s/a \ll 1$ refraction inhomogeneity localized near the core–cladding interface (Fig. 1) has almost no effect on the waveguide mode and its dispersion.

In the opposite limit of low v, the mode parameters are $u_0 \approx v$ and $w_0 \approx 1.12 \exp(-2/v^2)$ [green and red dashed lines in Fig. 2(a)], leading to $\Phi_0(v) \approx 10v^{-4}\exp(-4/v^2) = \Phi_c(v)$ [blue dashed line in Fig. 2(a)]. The solution for $\delta\beta_0$ is now approximated as $\delta\beta_0 \approx k\Delta n_a(s/a)\Phi_c(v)$. Even though, nominally, the fundamental mode has no cutoff at low v, it becomes so delocalized at $v \ll 1$ that it does not see much of the fiber core or the core–cladding boundary, with the normalized mode power confined to the fiber core being exponentially small, $\eta_0(v) \approx 1.3(v^2 + 2)v^{-4}\exp(-4/v^2)$.

Since in the limit of high v, the mode does not see much of the core–cladding interface either, because of its strong confinement within the fiber core, with $\eta_0(v \gg v_c) \approx 1 - u_{01}^2 v^{-3}\exp(-2/v)$, there should be an optimum in v that would maximize the overlap. Indeed, solving $d[\Phi_c(v)]/dv = 0$, we find $v_c = 2^{1/2}$. Such a value of v, however, falls beyond the range where low-v approximations of mode parameters, including $\Phi_0(v) \approx \Phi_c(v)$, are reasonably accurate [cf. solid and dashed blue lines in Fig. 2(a)]. To find the maximum of $\Phi_1(v)$ with a higher accuracy, we calculate this function using the general formula as $\Phi_0(v) = 2(u_0/v)^2 K_0^2(w_0)[K_1(w_0)]^{-2}$, with u_0 and w_0 found by numerically solving the relevant dispersion equation. At $v \ll 1$, this solution for $\Phi_0(v)$ is indistinguishable from $\Phi_c(v)$ [Fig. 2(a)]. As v increases, approaching $v \approx 1$, $\Phi_0(v)$ deviates from $\Phi_c(v)$, as expected, but continues to display a well-resolved maximum, exactly as $\Phi_c(v)$ does. The v value at which $\Phi_0(v)$ reaches its maximum, $v_m \approx 1.8$, is slightly shifted [Fig. 2(a)] relative to the peak of $\Phi_c(v)$ at $v_c \approx 2^{1/2}$. That Φ_0 has a maximum as a function of v implies the existence of a
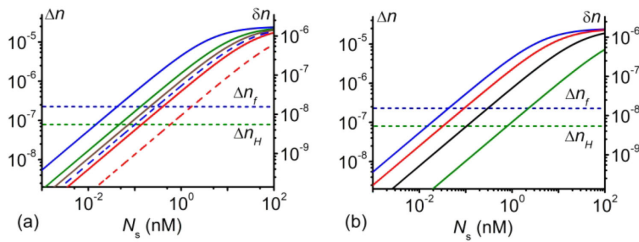
Fig. 3. Refractive index change Δn (left axis) and $\delta n_0 = \delta\beta_0/k$ (right axis) as functions of N_s at equilibrium for (a) different rate constants K_d of SARS-CoV-2 (solid curves) and SARS-CoV (dashed curves) spike protein RBD, as surveyed from Refs. [11,15–17] and (b) different temperatures T for $\Delta H_b \approx 73.3$ kcal/mol and $T_0 = 37°$C: (a) $K_d = 4.6$ nM [15] (blue solid line), 32 nM [15] (blue dashed line), 44.2 nM [16] (red solid line), 185 nM [16] (red dashed line), 14.7 nM [17] (green solid line), 23.2 nM [16] (brown line); (b) $T = 37°$C (blue curve), 35°C (red curve), 32°C (black curve), and 27°C (green curve). Also shown are the detection limits Δn_H (green dotted line) and Δn_f (blue dotted line).

---

universal condition for maximum $\delta\beta_0/\Delta n$, applicable to any circular fiber regardless of the specific values of n_1, n_2, and a. Any sensor within this class of waveguides will be optimized for a maximum $\delta\beta_0/\Delta n$ by adjusting its v parameter for $v_m \approx 1.8$.

We now relate Δn_a to a buildup of coronavirus S protein–ACE2 receptor complex on the waveguide surface (Fig. 1). Coronavirus S proteins are homotrimeric molecules [10] where each monomer has a molecular mass $M_s \approx 180$ kDa and includes two subunits, referred to as S1 and S2 (the inset in Fig. 1), whose role is, respectively, to mediate the attachment to a targeted cell and drive the membrane fusion. Binding to ACE2 receptors, coronavirus S proteins form protein–protein complexes via RBDs at their distal tips with typical dimensions [13,14] $d_1 \approx 229$ Å and $d_2 \approx d_3 \approx 105$ Å. For a conservative estimate, we set N_0 at a level within the bounds of typical surface densities of ligand–protein binding sites attainable in a standard ELISA experiment [10,13–16]. The rate equation for $N_c(t)$ can then be solved, subject to $N_r + N_c = N_0$, yielding $N_c(t) = k_1 N_0 N_s (k_1 N_s + k_2)^{-1}\{1 - \exp[-(\tau_1^{-1} + \tau_2^{-1})t]\}$, where $\tau_1 = 1/(k_1 N_s)$ and $\tau_2 = 1/k_2$. At equilibrium, $dN_c/dt = 0$, or $t \to \infty$, the solution for N_c is given by the Langmuir isotherm, $N_{c0} = K_a N_0 N_s/(1 + K_a N_s)$, where $K_a = k_1/k_2 = 1/K_d$ is the binding, or association constant, and K_d is the dissociation constant.

The refractive index change $\Delta n(t)$ induced by the buildup of $N_c(t)$ can be found in the general case by solving the Lorentz–Lorenz equation or a suitable refraction index mixing rule ssssequation [17,18]. Within the entire parameter space considered here, however, Δn is small, never exceeding $\sim 2 \cdot 10^{-5}$ [Figs. 2(a), 3(a), and 3(b)], making the linear approximation, $\Delta n \approx (dn/dN_m)N_c$, overwhelmingly accurate [12,19]. The refractive index increment dn/dN_m can generally vary for individual amino acids in proteins, reflecting variations in their polarizabilities. For mid-size and large proteins, however, these variations average out [12,19]. As a consequence, for naturally occurring proteins with a molecular mass above 100 kDa, the statistical distribution of dn/dN_m is close to a Gaussian with a center at $dn/dN_m \approx J_0 \approx 0.189$ ml/g and a standard deviation as low as 0.0025 ml/g [12].

Shown in Fig. 2(b) are three typical $N_c(t)/N_0$ curves for N_s densities taken at the low N_s end ($N_s = 5$ nM), a mid-N_s

point ($N_s = 20$ nM), and the high N_s end ($N_s = 100$ nM) of the SARS-CoV-2 RBD concentration range accessible with SPR, ELISA, and BI [10]. The rate constants in these calculations are chosen in such a way ($k_1 \approx 1.75 \cdot 10^5$ M^{-1}s^{-1} and $k_2 \approx 7.75 \cdot 10^{-3}$ s^{-1}) as to fit the SPR data for wild-type SARS-CoV-2 binding to hACE2 [13,14], yielding $K_d \approx 44.2$ nM, in full agreement with Shang *et al.* [14]. The $N_c(t)$ concentrations in Fig. 2(b) asymptotically evolve to their equilibrium values, N_{c0}, within a time scale $\tau_e \approx [\tau_1^{-1} + \tau_2^{-1}]^{-1}$, estimated as $\tau_e \approx 120$ s for $N_s = 5$ nM, $\tau_e \approx 90$ s for $N_s = 20$ nM, and $\tau_e \approx 40$ s for $N_s = 100$ nM, also in close agreement with experiments [16]. Also shown in Fig. 2(b) is the time-dependent refractive index change $\Delta n(t) = J_0 N_c(t)$ for $M_s \approx 180$ kDa, $d_1 \approx 229$ Å, $d_2 \approx d_3 \approx 105$ Å, and $J_0 \approx 0.19$ ml/g. For high N_s [$N_s = 0.1$ µM in Fig. 2(b)], the index change is seen to reach the $\Delta n \sim 10^{-5}$ level at $t \approx \tau_e$, a useful benchmark for Δn in this sensing arrangement, slowly increasing for larger t, to make it to $\Delta n \approx 1.7 \cdot 10^{-5}$ at $t \approx 100$ s.

Figure 3(a) plots Δn as a function of N_s at Langmiur isotherm equilibrium, i.e., in the $dN_c/dt = 0$ steady state. With the binding rate constants set at $k_1 \approx 1.4 \cdot 10^6$ M^{-1}s^{-1} and $k_2 \approx 6.5 \cdot 10^{-3}$ s^{-1}, as assessed from SPR studies of SARS-CoV-2–hACE2 binding [13], the equilibrium index change Δn is seen to overtake the $\Delta n_H \approx 8 \cdot 10^{-8}$ waveguide-sensing detection-limit borderline [7], with N_s just above 20 pM. The Δn of the protein monolayer, however, is not directly observable in our sensing scheme. Connecting it to an observable, viz., the phase shift, is the normalized ground-state eigenvalue shift $\delta n_0 = \delta\beta_0/k$. The highest N_s detection sensitivity can only be achieved in this scheme by working near the maximum of $\delta n_0/\Delta n \approx (s/a)\Phi_0(v)$.

However damaging it may be for the sensitivity, the s/a factor in $\delta n_0/\Delta n$ is now better appreciated as an inevitable cost for the fine specificity of protein sensing that becomes possible due to the confinement of protein receptor binding within a very thin, $s \approx d_1$ layer on the waveguide surface. Waveguides with small, perhaps, subwavelength cores could help reduce this cost. Such waveguides are routinely found in integrated optics. As one prominent example, a multichannel Young interferometer based on an integrated optic waveguide with a silicon nitride ($n_1 \approx 2.04$) core as small as $2a \approx 90$ nm has been shown to enable an unprecedented refractive index resolution at the level of $\Delta n_H \approx 8 \cdot 10^{-8}$ [7], setting a milestone for biosensing [green dotted line in Fig. 3(a)].

In tapered optical fibers, on the other hand, a robust guiding in sub-λ cores [20] can be combined with longer propagation paths, L, and are attainable within lower n_1 materials [21]. Specifically, for a silica fiber taper with $n_1 \approx 1.46$ and $2a \approx 0.4$ µm, surrounded by a standard biological buffer, such as phosphate buffer saline, with $n_2 \approx 1.34$, a standard blue diode laser wavelength $\lambda \approx 470$ nm converts to $v \approx 1.55$, where $\delta n_0/\Delta n$ is near its maximum, $\delta n_0/\Delta n \approx (d_1/a)\Phi_0(v) \approx 0.07$. The waveguide sensing detection limit at Δn_H will thus project onto a detection limit at $\Delta n_f \approx (1 - \eta_0)(a/d_1)[\Delta n_H/\Phi_0(v)]$ in our fiber-sensing setting. Since the limiting Δn sensitivities at the level of $\Delta n_H \approx 8 \cdot 10^{-8}$ are achieved with integrated optic waveguide interferometers, with η_0 of ≈ 0.7 to 0.8, the detection cutoff for our sensor is at Δn_f of $\approx 2.3 \cdot 10^{-7}$ to $3.4 \cdot 10^{-7}$, as shown by the blue dotted line in Fig. 3(a).

The equilibrium, Langmuir isotherm plots of $\Delta n(N_s)$ and $\delta n_0(N_s)$ in Fig. 3(a), represent a variety of the binding rate constants of SARS-CoV-2 (solid curves) and SARS-CoV (dashed

curves) spike proteins, as surveyed from the latest SARS-CoV literature [10]. Even though K_d readings tend to vary from one experiment to another, sometimes showing a sensitivity to the method of K_d characterization [10], the general consensus with regard to SARS-CoV-2 is that the K_d constants for this virus are significantly lower than the respective K_d values for SARS-CoV, indicating a much higher binding affinity of the SARS-CoV-2 S protein to hACE2. This important finding highlights, once again, the necessity of in-depth studies and a careful quantitative kinetic and thermodynamic characterization of the receptor binding affinity of SARS-CoV-2 spike proteins within a broad range of N_s and N_0, and as a function of thermodynamic variables. With its Δn detection limit at $\approx 2.3 \cdot 10^{-7}$ to $3.4 \cdot 10^{-7}$, the fiber-taper sensor, is seen to be well suited for such studies within the $\sim$10- to $\sim$100 pM range of SARS-CoV-RBD concentrations, well below N_s levels accessible to standard protein receptor binding characterization methods.

We emphasize that our analysis of Δn sensitivity is based on a conservative estimate for N_0, which is set here at a moderate level within the bounds of typical surface densities of ligand–protein binding sites attainable in a standard ELISA experiment. With N_0 taken at the level of the maximum ligand surface densities attainable with the cutting-edge technologies of antibody immobilization, two to three orders of magnitude higher Δn sensitivities are foreseeable for the considered fiber-optic sensor.

Connection to the thermodynamics of SARS-CoV-RBD–ACE2 binding is revealed via the reaction isotherm equation, $K_a = 1/K_d = C_0^{-1} \exp[-\Delta G_b / (RT)]$, where T is the temperature, R is the universal gas constant, $\Delta G_b = \Delta H_b - \Delta S_b T$ is the Gibbs free energy change (also referred to as the binding free energy, or the binding affinity), ΔH_b and ΔS_b are the binding enthalpy and entropy, respectively, and C_0 is a reference concentration. As an important insight into the higher hACE2 binding affinity of SARS-CoV-2 S proteins, molecular-docking and molecular-dynamics simulations predict [22] that the Gibbs free energy of S protein–hACE2 binding for SARS-CoV-2, $|\Delta G_b| \approx 13.76$ kcal/mol is substantially higher than the $|\Delta G_b|$ of S protein–hACE2 binding for SARS-CoV, $|\Delta G_b| \approx 8.65$ kcal/mol.

For an experimental characterization of SARS-CoV-RBD–ACE2 binding thermodynamics, the equilibrium binding isotherm $N_{c0} = K_a N_0 N_s / (1 + K_a N_s)$ has to be measured at two temperatures, T_1 and T_2, yielding two association constants, K_{a1} and K_{a2}. Combining the reaction isotherm equations for T_1 and T_2, we arrive at the integral of the van't Hoff equation, $\ln(K_{a2}/K_{a1}) = -(\Delta H_b/R)(1/T_2 - 1/T_1)$. Recent detailed experimental studies by Zhou *et al.* [23] suggest that, at physiological pH, the binding enthalpy of the SARS-CoV-2 spike protein is $\Delta H_b \approx 73.3$ kcal/mol. With such a binding enthalpy, a physiologically significant temperature alteration of 0.1°C relative to a baseline temperature $T_0 = 37^\circ$C will translate into a $\Delta n_T \approx 10^{-6}$ change in Δn, which is still within the Δn resolution of the waveguide sensor. Temperature changes thus allow a reliable quantitative thermodynamic characterization of the SARS-CoV-2 spike protein [Fig. 3(b)].

To summarize, we have shown that a local change in the dielectric function of a medium induced by protein binding to a receptor can be read out optically, with a suitably designed optical waveguide, enabling an optical detection and quantitative characterization of coronavirus spike glycoprotein–host-receptor binding. We have developed a closed-form framework for a quantitative description of such a readout, combining wave equation analysis of waveguide mode eigenvalues, with the kinetic and thermodynamic treatment of the binding reaction.

REFERENCES

1. P. Russell, Science **299**, 358 (2003).
2. A. M. Zheltikov, Phys. Usp. **43**, 1125 (2000).
3. J. M. Dudley, G. Genty, and S. Coen, Rev. Mod. Phys. **78**, 1135 (2006).
4. T. Udem, R. Holzwarth, and T. W. Hänsch, Nature **416**, 233 (2002).
5. T. Balciunas, C. Fourcade-Dutin, G. Fan, T. Witting, A. A. Voronin, A. M. Zheltikov, F. Gerome, G. G. Paulus, A. Baltuska, and F. Benabid, Nat. Commun. **6**, 7117 (2015).
6. A. M. Zheltikov and M. O. Scully, "Photon entanglement for life science imaging: rethinking the limits of the possible," Phys. Usp., doi: 10.3367/UFNe.2020.03.038743.
7. A. Ymeti, J. Greve, P. V. Lambeck, T. Wink, S. W. F. M. van Hövell, T. Beumer, R. R. Wijn, R. G. Heideman, V. Subramaniam, and J. S. Kanger, Nano Lett. **7**, 394 (2007).
8. S. Faez, Y. Lahini, S. Weidlich, R. F. Garmann, K. Wondraczek, M. Zeisberger, M. A. Schmidt, M. Orrit, and V. N. Manoharan, ACS Nano **9**, 12349 (2015).
9. L. He, Ş. K. Özdemir, J. Zhu, W. Kim, and L. Yang, Nat. Nanotechnol. **6**, 428 (2011).
10. A. C. Walls, Y.-J. Park, M. A. Tortorici, A. Wall, A. T. McGuire, and D. Veesler, Cell **181**, 281 (2020).
11. A. W. Snyder and J. D. Love, *Optical Waveguide Theory* (Springer, 1983).
12. H. Zhao, P. H. Brown, and P. Schuck, Biophys. J. **100**, 2309 (2011).
13. J. Lan, J. Ge, J. Yu, S. Shan, H. Zhou, S. Fan, Q. Zhang, X. Shi, Q. Wang, L. Zhang, and X. Wang, Nature **581**, 215 (2020).
14. J. Shang, G. Ye, K. Shi, Y. Wan, C. Luo, H. Aihara, Q. Geng, A. Auerbach, and F. Li, Nature **581**, 221 (2020).
15. M. Yuan, N. C. Wu, X. Zhu, C.-C. D. Lee, R. T. Y. So, H. Lv, C. K. P. Mok, and I. A. Wilson, Science **368**, 630 (2020).
16. D. Wrapp, N. Wang, K. S. Corbett, J. A. Goldsmith, C.-L. Hsieh, O. Abiona, B. S. Graham, and J. S. McLellan, Science **367**, 1260 (2020).
17. T. P. Dale and J. H. Gladstone, Philos. Trans. R. Soc. **148**, 887 (1858).
18. O. Wiener, Ber. Akad. Wiss. Leipzig **62**, 256 (1910).
19. E. J. Cohn and J. T. Edsall, *Proteins, Amino Acids and Peptides* (Van Nostrand Reinhold, 1943).
20. D. A. Akimov, A. A. Ivanov, M. V. Alfimov, S. N. Bagayev, T. A. Birks, W. J. Wadsworth, P. St.J. Russell, A. B. Fedotov, V. S. Pivtsov, A. A. Podshivalov, and A. M. Zheltikov, Appl. Phys. B **74**, 307 (2002).
21. D. A. Akimov, A. A. Ivanov, A. N. Naumov, O. A. Kolevatova, M. V. Alfimov, T. A. Birks, W. J. Wadsworth, P. St.J. Russell, A. A. Podshivalov, and A. M. Zheltikov, Appl. Phys. B **76**, 515 (2003).
22. J. de Andrade, P. F. B. Gonçalves, and P. A. Netz, "How does the novel coronavirus interact with the human ACE2 enzyme? A thermodynamic answer," ChemRxiv. Preprint. chemrxiv.12361238.v2 (2020).
23. T. Zhou, Y. Tsybovsky, A. S. Olia, J. Gorman, M. A. Rapp, G. Cerutti, P. S. Katsamba, A. Nazzari, J. Bimela, A. Schön, P. Wang, W. Shi, I.-T. Teng, B. Zhang, J. C. Boyington, G.-Y. Chuang, J. M. Sampson, M. Sastry, T. Stephens, J. Stuckey, S. Wang, R. A. Friesner, D. D. Ho, J. R. Mascola, L. Shapiro, and P. D. Kwong, "A pH-dependent switch mediates conformational masking of SARS-CoV-2 spike," bioRxiv 2020.07.04.187989 (2020).